1st AO4ELT conference, 08005 (2010)
DOI:10.1051/ao4elt/201008005

Laboratory Experiments of Laser Tomographic Adaptive Optics at Visible Wavelengths on a 10-meter Telescope

S. Mark Ammons[1,a,b], Luke Johnson[2], Don T. Gavel[2], Renate Kupke[2], and Claire E. Max[2]

[1] University of Arizona, 933 Cherry Ave., Tucson AZ 85721 USA
[2] Center for Adaptive Optics, 1156 High St., Santa Cruz, CA 95064 USA

Abstract. We review laboratory experiments of Laser Tomographic Adaptive Optics (LTAO) and Multi-Object Adaptive Optics (MOAO) on a simulated 10-meter telescope testbed at 710 nm. The system maintains 20-35% Strehl across 45 arcseconds over the equivalent of 0.8 seconds of operation. New results are presented at a variety of simulated wavelengths following a system upgrade to 85x85 subapertures across a 10-meter pupil. The delivered PSF is nearly diffraction-limited at wavelengths as blue as 425 nm.

1 Introduction

Adaptive Optics (AO) as exploited for astronomical observations has traditionally been limited by three crucial shortcomings: (1) Incomplete wavelength coverage (i.e., only at infrared wavelengths); (2) Insufficient sky coverage; and (3) Reduced Field-of-View (FOV). Several new adaptive optics architectures promise improvements in these three areas.

Laser Tomographic Adaptive Optics (LTAO) utilizes multiple laser guide stars (LGS) to improve wavefront sensing accuracy in a single direction [1][2][3]. For certain narrow LGS constellation geometries, tomographic analysis of LGS wavefronts removes the "cone effect" error endemic to traditional LGS-AO systems. Multi-Object Adaptive Optics (MOAO) is an extension of LTAO in which the LGS constellation is widened to achieve a larger field. Correction is simultaneously achieved in multiple directions with individual deformable mirrors that pick off light from separate field points [4].

Removing the "cone effect" error with multiple guide stars will be critical for achieving good correction at visible wavelengths on large telescopes with appreciable sky coverage, as this error term may be as high as $\sim$ 150 nm RMS for 8-10 meter apertures. To date, the LTAO and MOAO architectures have not been explored with integrated instruments on telescopes.

We review laboratory experiments of LTAO, and MOAO indirectly, on the LTAO/MOAO testbed in the Laboratory for Adaptive Optics at UCSC. This instrument uses 66x66 subaperture wavefront sampling and high-order deformable mirrors to investigate LTAO performance at 710 nm, or R-band. Over the equivalent of 0.8 seconds of operation, the system maintains 20-35% Strehl at this science wavelength over a 45 arcsecond FOV. We then present new experimental results at a variety of simulated science wavelengths, extending as blue as 425 nm. These new tests utilize an upgraded wavefront sensor with 85x85 subapertures across the illuminated pupil. We present the testbed optical layout in Section 2, review its performance at 710 nm in Section 3, discuss the error budget in Section 4, present new experiments at bluer wavelengths in Section 5, and conclude in Section 6.

2 Laser Tomographic / Multi-Object AO Testbed

The Laser Tomographic / Multi-Object AO (LTAO/MOAO) testbed is an integrated demonstrator of wide-field adaptive optics. A schematic of the testbed is shown in Figure 1. Further details of the testbed construction and performance are given in previous publications [5][6][7].

[a] e-mail: ammons@as.arizona.edu
[b] Hubble Fellow

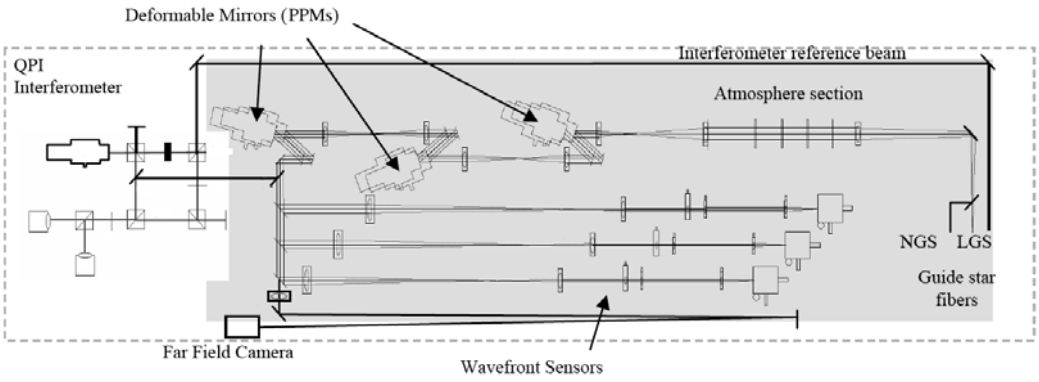

Fig. 1. Schematic of testbed optical layout. Reproduced from Figure 3 in [7].

The testbed uses five LEDs in a "box-5" or "quincunx" arrangement to simulate laser guide stars at an equivalent altitude of 90 km. Seven science test stars are generated with a diode laser at 658 nm. A moving atmosphere is simulated with 3 translatable glass, acrylic, or plastic slides fixed to Galil motors, at equivalent elevations of 0, 4.5, and 9 km.

The testbed uses Hamamatsu Programmable Phase Modulators (PPM) as deformable mirrors (DM), which consist of internal liquid-crystal screens that are used to control phase in reflection. These deformable mirrors are limited in spatial resolution only by the pixel size (768x768), and can be controlled at lower resolution to simulate any desired DM influence function. For LTAO experiments, a single deformable mirror conjugate to the telescope pupil is used.

Five star-oriented Shack-Hartmann wavefront sensors (WFS) are optically multiplexed onto two Dalsa cameras with 66x66 subapertures across a 10-meter pupil (upgraded to 85x85 in later simulations). The LGS constellation has an equivalent diameter of 45 arcseconds when the Hartmann sensor is sampled at 66x66 subapertures and a diameter of 35 arcseconds in 85x85 mode. Each Hartmann spot (0.61 pixels full-width at half-maximum (FWHM)) is imaged onto 4x4 pixel subarrays for centroiding.

The Hartmann sensors operate in open-loop with an accuracy of 30 nm RMS for typical piston/tip/tilt-removed atmospheric disturbances of RMS $\sim$ 600 nm, obtained with repetitive calibration of Hartmann linearity. This calibration is performed by raster-scanning the laser guide star constellation while recording Hartmann spot offsets. These signals are inverted and stored to enable a look-up of unbiased tilt for any measured signal during operation. For more details on linearity calibration, see references [5][7].

Details of software implementation are presented in previous publications [5,8]. Simple center of mass centroiding is used to reconstruct slopes, which are reconstructed into phase with an iterative FFT-based reconstructor [9]. The five LGS wavefronts are analyzed tomographically to yield phase as a function of atmospheric height [10]. Wavefronts at multiple field points are predicted with line integrals through this data cube. These wavefronts are mapped onto the physical deformable mirror, wrapping phase at 2π intervals to avoid stroke saturation. Performance is checked with point sources (at infinite distance) interspersed throughout the field. Full MOAO operation is simulated by freezing the atmosphere and applying optimized corrections for different field points separately [7].

3 LTAO/MOAO Performance at R-band

To simulate performance on a telescope, three atmospheric layers are set to emulate a Mauna Kea-like atmospheric strength and distribution. The D/r_0 strengths of these layers simulate a science wavelength of 710 nm, which is very close to the physical laser wavelength of 658 nm.

The 0.8 second simulation is split into four realizations, with slightly different wind speeds (varying from 5 to 20 m/s). The mean θ_0 and r_0 over the full simulation is 3.17 arcseconds and 16.2 cm at 500 nm, respectively. The time-integrated point spread functions during the AO simulation are shown

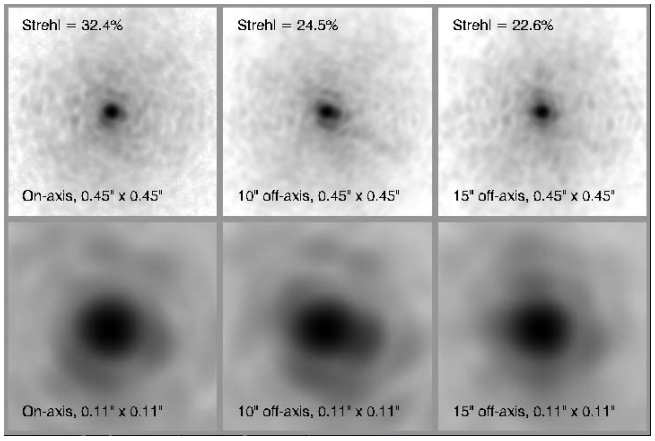

Fig. 2. Time-averaged Point Spread Functions for the MOAO simulation at a science wavelength of 710 nm. All panels are log scaled. Bottom frames are zoomed-in by a factor of four with respect to the top frames. The left panels denote integrated PSFs on-axis, the center panels show PSFs at 10 arcseconds off-axis, and the right panels show PSFs at 15 arcseconds off-axis. This figure is reproduced from Figure 7 of reference [7].

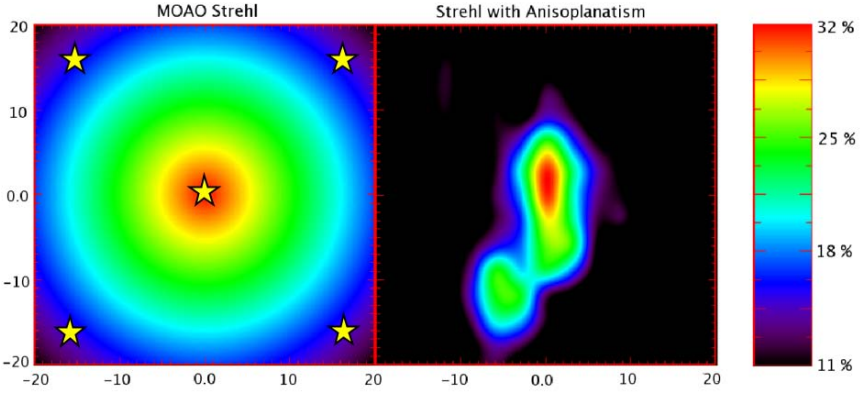

Fig. 3. Left: Fitted MOAO strehl distribution for 40"x40" field of view. Right: Strehl distribution including the effects of anisoplanatism and not the cone effect. The anisoplanatic Strehl map is obtained as in [7]. LGS positions are denoted by small yellow stars.

in Figure 2. The spatial Strehl distribution for this experiment is shown in Figure 3. Note that multiple scientific detectors with embedded DMs would be necessary to realize this Strehl distribution at a single instant [7].

4 Error Budget Model

We compose a complete time- and space-dependent error budget model comprising 13 individual error terms, either checked with independent interferometric methods or backed with simulation (see Table 1). Using as input only the distribution of atmospheric strength as a function of simulated time, this model correctly predicts the on-axis Strehl to 3%, but overpredicts the off-axis Strehl by 16%. We attribute this overprediction to a spatially dependent error propagator in the tomographic analysis algorithm, i.e., wavefront measurement errors propagate to larger tomographic error in the outer rings of upper altitude metapupils than in the inner pupil. This effect was not included in the error budget model [7].

We group error budget terms into three categories: Traditional (fitting, tomographic, photon error, wavefront aliasing, and scintillation); Calibration (WFS open-loop error, DM go-to error, static uncorrectable, and WFS scintillation); and Dynamic drift (pupil registration drift, linearity calibration decay, and WFS zeropoint drift). We find that the total magnitude of errors involving calibration and optical drift is comparable to the total magnitude of traditional error terms.

Table 1. Error budget for 10 meter case at 710 nm. Each term represents the mean over all 160 AO iterations over 4 atmospheric realizations. All values are in units of nanometers, unless otherwise stated. The left column gives error budget values in on-sky units on-axis. The middle column gives values in on-sky units at an off-axis distance of 12.5″. The right column displays error budget values in physical, laboratory units (unstretched) for the on-axis case. Table reproduced from Table 3 of [7].

Error Budget Term	On-sky, on-axis	On-sky, off-axis (12.5″)	Lab, on-axis (658 nm)
Fitting Error	40.7	40.7	37.7
WFS Aliasing	16.2	16.2	15.0
Tomography Error	69.0	83.8	63.9
WFS Systematic error	41.5	41.5	38.5
Field Stop Misalignment	10.8	10.8	10.0
PPM Lookup Table error	32.4	30.0	30.0
Static Uncorrectable, S=83%	48.6	45.0	45.0
Scintillation	12.6	12.6	11.7
WFS Scintillation	26.8	26.8	24.8
Photon error	16.2	16.2	15.0
WFS zeropoint drift	10.8	10.8	10.0
Linearity calibration drift	10.8	10.8	10.0
Pupil registration drift	25.9	25.9	24.8
Total RMS	118.2	127.3	109.5
Predicted Strehl (%)	33.5	28.1	33.5
Measured Strehl (%)	32.4	23.6	32.4
Relative Error in Model	3.3%	16.0%	3.3%

5 LTAO/MOAO Performance at Blue Wavelengths

We now present recent experimental results at a simulated science wavelength of 425 nm (*B*-band). As mentioned in Section 3, the physical D/r_0 strength of the atmosphere can be manipulated to simulate different science wavelengths or different seeing quality (i.e., $r_{0,500}$; see section 3.2 in [7]) when the telescope diameter is kept fixed at 10 meters. This new experiment uses a D/r_0 strength of 74, almost a factor of 2 larger than in the R-band experiments presented in section 3. The atmosphere has a Mauna Kea-like C_N^2 height distribution and low wind speeds of $\sim$ 10 m/s. We utilize an upgraded wavefront sensor of 85x85 subapertures across a 10-m pupil, which in turn increases the number of degrees of freedom available to the deformable mirror to 85x85. All wavefront sensing, tomographic processing, and deformable mirror control is performed as described in Section 2.

The on-axis Strehl for this experimental setup is 10% and the off-axis (8-12") Strehls are 5-8% over a 200 millisecond simulation. The PSFs images at multiple field positions are shown in Figure 4;

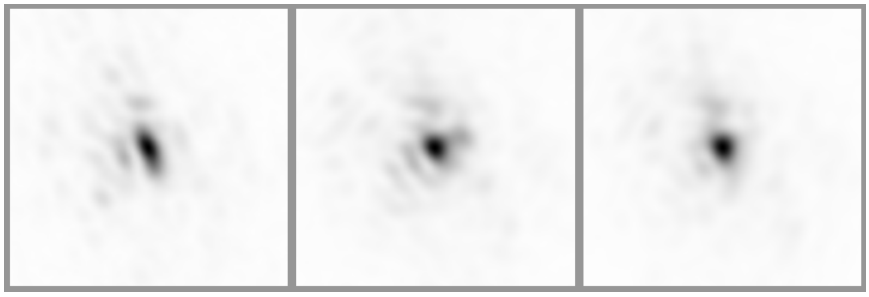

Fig. 4. Point spread functions for 200 millisecond simulation with 85x85 subaperture wavefront sensors. The left panel is on-axis, the middle panel is the mean PSF 8" off-axis, and the right panel is the mean PSF 12" off-axis. Note that the diffraction-limited core is retained at all field positions. Images are 0.17" across with linear stretch.

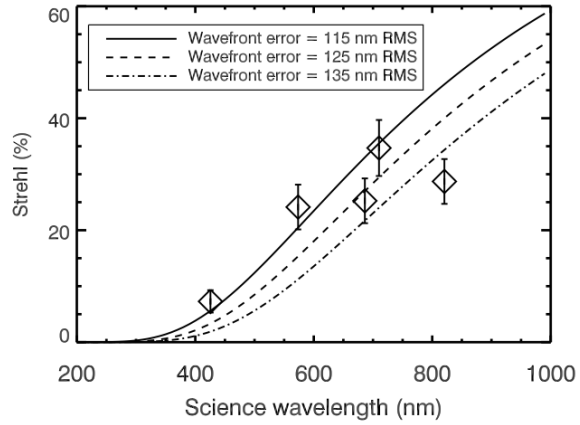

Fig. 5. Strehl as a function of simulated science wavelength for five 200 millisecond simulations. The four rightmost points are taken from the simulations reviewed in Section 3 (66x66 Hartmann sensor), with science wavelength chosen to correspond to a fixed $r_{0,500\,nm}$ of 16 cm. The leftmost point is taken from recent simulations with a 85x85 Hartmann sensor. Strehl predictions for varying fixed amplitudes of wavefront error under the Mareschal approximation are shown as dashed and solid lines.

note that the diffraction-limited core is visible, although widened, at this simulated science wavelength of 425 nm. Residual error in tip/tilt (not simulated here) would be expected to wash out these cores further.

Figures 5 and 6 display the measured Strehls, FWHM's, and 50 mas ensquared energies of this simulation as well as the R-band simulations reviewed in Section 3. We re-analyze the R-band experimental results to vary the simulated science wavelength instead of seeing quality ($r_{0,500\,nm}$) for the four realizations of different atmospheric amplitude D/r_0. Notice that the Strehl distributions in Figure 5 approximately match the expectation for a fixed wavefront error of 125 nm RMS. The B-band point (425 nm) was obtained under an improved experimental setup than the redder points (85x85 subapertures compared to 66x66).

The behavior of the FWHM as a function of wavelength displays a characteristic minimum of about $\sim$ 16 milliarcseconds at 500 nm (Figure 6a). Taking into account an expected tip/tilt residual of 15 milliarcseconds RMS on-sky for bright tip/tilt stars, this suggests that FWHM's of $\sim$ 20 milliarcseconds may be possible on a 10-meter telescope with an LTAO system of this order. Note that the FWHM values for simulated science wavelengths redder than 500 nm are typically within 25% of diffraction-limited. As shown in Figure 6b, the ensquared energy for a fixed spaxel size of 50 milliarcseconds is flat as a function of wavelength with a dropoff at blue wavelengths ($\sim$ 500 nm).

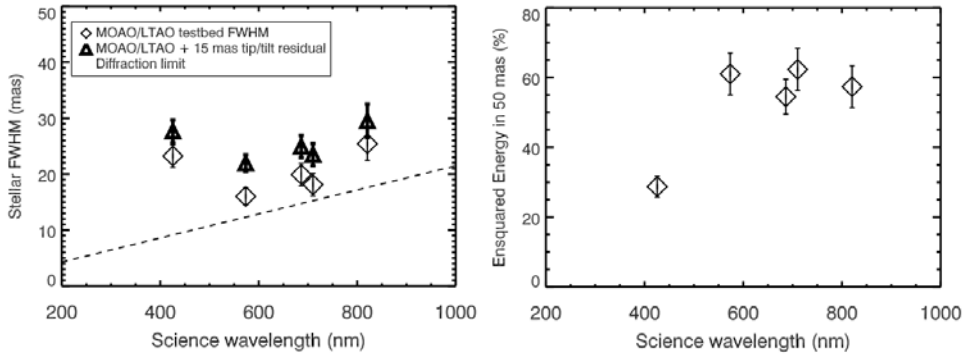

Fig. 6. Left: PSF full-width at half-max (FWHM) as a function of science wavelength. Diamonds denote measured values and triangles mark values convolved with a 15 milliarcsecond tip/tilt residual. The dashed line is the diffraction-limited FWHM. Right: PSF ensquared energy in a 50 milliarcsecond spaxel as a function of wavelength. As in Figure 5, the four rightmost points are taken from the simulations reviewed in Section 3 (66x66 Hartmann sensor), with science wavelength chosen to correspond to a fixed $r_{0,500\ nm}$ of 16 cm. The leftmost point is taken from recent simulations with a 85x85 Hartmann sensor.

6 Conclusions

We have used a high-order adaptive optics system with multiple guide stars to simulate Multi-Object and Laser Tomographic Adaptive Optics on a 10-meter telescope at visible wavelengths. The system is close to diffraction-limited at wavelengths as blue as 425 nm when the subaperture size is reduced to 12 cm (85x85 subapertures). Close inspection of the error budget reveals that summed amplitude of all error terms involving calibration or optical drift are comparable to the total of all traditional error terms. This argues for the provision of extensive calibration facilities on future AO systems that intend to operate at visible wavelengths, including accelerometers on powered optics, full LGS and telescope simulators, and three-dimensional turbulators.

References

1. R. Ragazzoni, et al., A&A, **342**, (1999), p. 53.
2. E. Viard, et al., in Adaptive Optical Systems Technology, ed. P. Wizinowich, Proceedings of the SPIE, **4007**, (2000), p. 94.
3. A. Tokovinin, et al., A&A, **378**, (2001), p. 710.
4. F.F. Assémat, et al., in Optics in Atmospheric Propagation and Adaptive Systems VI., ed. J. Gonglewski and K. Stein, Proceedings of the SPIE, **5237**, (2004) p. 211.
5. S.M. Ammons, et al., in Astronomical Adaptive Optics Systems and Applications III, ed. R. Tyson and M. Lloyd-Hart, Proceedings of the SPIE, **6691**, (2007) p. 669108.
6. E. Laag, et al., JOSA A, **25**, (2008), p. 2114.
7. S.M. Ammons, et al., submitted to PASP, astro-ph/0901:1716, (2009).
8. S.M. Ammons, et al., in Advances in Adaptive Optics II., ed. B. Ellerbroek and D. Bonaccini Calia, Proceedings of the SPIE, **6272**, (2006) p. 627202.
9. L. Poyneer, et al., JOSA A, **19**, (2002), p. 2100.
10. D.T. Gavel, in Advancements in Adaptive Optics, ed. D. Bonaccini Calia, B. Ellerbroek, and R. Ragazzoni, Proceedings of the SPIE, **5490**, (2004) p. 1356.